AIAA SciTech Forum
11–15 & 19–21 January 2021, VIRTUAL EVENT
AIAA Scitech 2021 Forum

10.2514/6.2021-0121

Wavelet-based Optical Flow Velocimetry (wOFV) Applied to Tagging Velocimetry Data

T. S. Gevelber,* B. E. Schmidt†
Case Western Reserve University, Cleveland, OH 44106, USA
M. A. Mustafa,‡ D. Shekhtman,§ N. J. Parziale¶
Stevens Institute of Technology, Hoboken, NJ 07030, USA

This paper presents the application of wavelet-based optical flow velocimetry (wOFV) to tagging velocimetry image data. wOFV is demonstrated to compare favorably to cross-correlation on experimental two-dimensional Krypton Tagging Velocimetry (KTV-2D) images from a Mach 2.75 turbulent shock wave-boundary layer interaction. Results from both methods show good agreement for the mean velocity field, while wOFV has several advantages compared to cross-correlation including increased spatial resolution as well as robustness and simplicity of implementation. The performance of wOFV on tagging velocimetry images is evaluated quantitatively using a set of synthetic data including images and specified velocity fields. wOFV is highly accurate in regions of the images near the intersection of write lines, with median error vector magnitudes below 5%. Errors in the instantaneous measurements of the velocity fluctuations and vorticity are higher, with median values between 20 and 50%.

I. Introduction

Understanding the complex physics of turbulence in high-speed flows is critical to enable prediction of aerothermodynamic loads on hypersonic vehicles. This is already a challenging task, and the presence of shock waves adds significant complexity to the problem. Shock wave/turbulent boundary layer interactions (SWBLI) are characterized by unsteady separation of the boundary layer and increased turbulence fluctuations.[1,2]

Experimental measurements of the flow velocity in SWBLI are necessary to fully characterize this complex phenomenon. Two of the most common velocimetry techniques for fluid flows are laser doppler velocimetry (LDV)[3] and particle image velocimetry (PIV).[4] Both of these methods rely on seeding the flow with small tracer particles, which are assumed to faithfully follow the flow. It has been demonstrated, however, that this assumption can fail in low-density flows with large velocity fluctuations, such as turbulent hypersonic flows.[5,6]

Tagging velocimetry (TV) methods are an alternative to LDV and PIV for high-speed flows.[7] Instead of seeding the flow with small solid or liquid particles, TV tracks the fluorescence of excited gas molecules (or atoms) in the flow. The excited gas can be native, seeded or synthesized, and because the tracer is a gas, there are no issues associated with particle lag as there are for LDV and PIV in high-speed flows. A multitude of TV methods exist depending on the excited species and the method of excitation. Although the experimental details can be quite different for the various TV techniques, the resulting images are similar and so the processing methodology developed in this work could likely be applied to data from any TV method with minimal modifications. Much like PIV, TV methods produce an initial "write" image and a

*Undergraduate Researcher, CWRU Mechanical and Aerospace Engineering, 2123 Martin Luther King Jr. Drive, AIAA Student Member.
†Assistant Professor, CWRU Mechanical and Aerospace Engineering, 2123 Martin Luther King Jr. Drive, AIAA Senior Member.
‡Post Doctoral Researcher, Stevens Mechanical Engineering, 1 Castle Point Terrace, AIAA Member.
§Graduate Researcher, Stevens Mechanical Engineering, 1 Castle Point Terrace, AIAA Student Member.
¶Associate Professor, Stevens Mechanical Engineering, 1 Castle Point Terrace, AIAA Senior Member.

second "read" image of the excited gas molecules separated by a short time interval Δt. The displacement of the molecules is determined from the image pair, and it is interpreted as a velocity by dividing by the prescribed Δt.

The specific TV method examined in this work is Krypton Tagging Velocimetry (KTV). First demonstrated by Parziale et al.,[8] KTV excites krypton atoms in a mixture of nitrogen and krypton. Typically, the krypton concentration is low, on the order of 1%, so that the flow can be considered pure nitrogen; any small changes in transport properties may be easily calculated. The experimental data in this work comes from the application of KTV to a SWBLI in a Mach 2.75 flow with a 24° compression corner. The krypton is excited along lines produced by a pulsed-tunable laser. The single laser beam is split and formed into a two-dimensional grid using a beam splitter and a microlens array to allow two-dimensional measurements of the flow velocity. Details concerning the experiment are given by Mustafa et al.[9]

The image data from the resulting two-dimensional KTV (KTV-2D) method is substantially more difficult to analyze in order to extract velocity information compared to the one-dimensional data from previous studies. Mustafa et al.[9] use a complex procedure to identify the points of intersections in the grids in the write and read images, and then calculate the displacement by cross-correlation. One velocity vector is produced for each intersection that can be clearly identified *in both the write and read images*. Besides the complexity of the procedure and the requirement for manual inspection of the data, spatial resolution is sacrificed because much more information concerning the displacement of tracers (i.e. velocity) is present in the images than is extracted by calculating only the displacement of the points of intersection on the grids. Other researchers have also sought solutions to finding the translation of grid intersections. This includes the "spatial correlation technique" from Gendrich and Koochesfahani,[10] the "template matching method" from Ramsey and Pitz,[11] and the "Hough transform method" from Sánchez-González et al.[12]

A potential improvement on these methods is to analyze the 2D TV images with wavelet-based optical flow velocimetry (wOFV). wOFV is a method that uses optical flow to determine displacements between image pairs in fluid flows. It is applicable to any type of image, so long as they have identifiable features. It has been successfully applied to particle images, such as those produced by PIV,[13,14] as well as continuous scalar images from a simulated planar-laser induced fluorescence (PLIF) experiment.[15] wOFV computes displacements by assuming the conservation of brightness (intensity) between images in an image pair, and minimizing the difference between them. It is a so-called "dense" velocimetry method, meaning that it produces one velocity vector at each pixel in the images. This allows spatial turbulence spectra and derivative quantities, such as divergence, vorticity, and strain rate to be calculated.

wOFV analysis has the potential to extract substantially more information from the write and read images than previous approaches, because it is able to use entire lines of the excited krypton which make up the grid rather than just the intersection points of lines. Furthermore, it obtains velocity information in the immediate vicinity of intersection points, rather than a single vector at the center of the intersection, because the intersection occupies several pixels in the write and read images. This could possibly allow the computation of quantities such as vorticity at the intersection points, which would be of substantial value in understanding the turbulence characteristics in this flow.

II. Methods

A. Experiment

The experiments were performed in the AEDC Mach 3 Calibration Tunnel (M3CT) in Silver Spring, MD. The tunnel is comprised of a large vacuum tank attached to a converging diverging nozzle. A flexible isolation bag was added upstream of the orifice to contain the 99% N_2/1% Kr gas mixture. The flexibility ensured that the mixture stayed at constant ambient pressure. A valve is cycled downstream of the nozzle to run the tunnel. The geometries chosen were a flat-plate boundary layer and a shock-wave/turbulent boundary-layer interaction with a turning angle of 24°. Conditions are listed in Table 1.

As described in Sec. I, the KTV-2D method generates images to compare over a known time interval by seeding the flow with krypton and exciting the atoms with a grid of tunable laser light. As the krypton is excited, the write image is captured. Because the write image captures the initial excitement of the krypton particles, all write images are very nearly identical and are averaged together. A short time after the write image is taken, the same krypton particles are re-excited by the read laser and the read image is captured. Based on the displacement of the line crossings of the grids, the velocity at various points in the flow field can be determined.

KTV is performed in the following steps according to the energy level diagram shown in Fig. 1. Note that this excitation is an improvement over early KTV efforts[8,9,16–18] and since this time the KTV write/read scheme has been significantly simplified.[19–21]

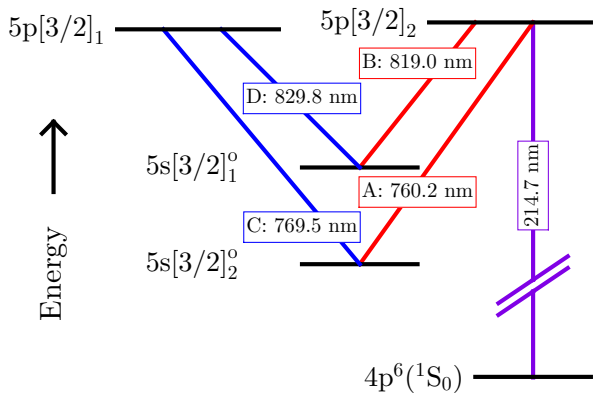

Figure 1: Energy diagram for excitation scheme. Racah nl[K]$_J$ notation, A, B, C and D represent the transitions between the states.

1. Seed a base flow with krypton globally.

2. Photosynthesize metastable krypton atoms with a pulsed tunable laser to form the tagged tracer: two-photon excitation of $4p^6(^1S_0) \rightarrow 5p[3/2]_2$ (214.7 nm) and rapid decay to resonance state $5p[3/2]_2 \rightarrow 5s[3/2]^o_1$ (819.0 nm, transition B) and metastable state $5p[3/2]_2 \rightarrow 5s[3/2]^o_2$ (760.2 nm, transition A). We estimate that the creation of the metastable atoms which comprise the "write line" takes approximately 50 ns.[22] The position of the write line is marked by the fluorescence from the $5p[3/2]_2 \rightarrow 5s[3/2]^o_1$ transitions (819.0 nm, transition B), and is recorded with a camera positioned normal to the flow.

3. Record the displacement of the tagged metastable krypton by imaging the laser induced fluorescence (LIF) that is produced with an additional pulsed tunable laser: excite $5p[3/2]_1$ level by $5s[3/2]^o_2 \rightarrow 5p[3/2]_1$ transition with laser sheet (769.5 nm, transition C) and read spontaneous emission of $5p[3/2]_1 \rightarrow 5s[3/2]^o_1$ (829.8 nm, transition D) transitions with a camera positioned normal to the flow.

The experiment was run using two tunable lasers to provide the 214.7 nm (write) and 769.5 nm (read) laser beams required for KTV (schematic in Fig. 2). The write laser consisted of a frequency doubled Quanta Ray Pro-350 Nd:YAG laser and a frequency tripled Sirah PrecisionScan Dye Laser. The Nd:YAG laser pumped the dye laser with 1000 mJ/pulse at a wavelength of 532 nm. The dye in the laser was DCM with a dimethyl sulfoxide (DMSO) solvent, and the laser was tuned to output a 644.1 nm beam. Frequency tripling of the dye-laser output was performed using Sirah tripling optics (THU 205).

The write-laser beam setup can result in approximately 10-13 mJ/pulse; however, approximately 7 mJ was used for this experiment by reducing the Nd:YAG pump-laser power. The wavelength was 214.7 nm, with a linewidth of approximately 0.045 cm^{-1}, a pulsewidth of approximately 7 ns, and a repetition rate of 10 Hz. The write-laser beam was split into two beams with a beam splitter designed for use with a 193 nm Excimer laser (Lambda Research XPR-SWI-4002U-50R-193-45U). To evenly split the laser beams the

Table 1: M_∞, P_∞, T_∞, ρ_∞, $\mathrm{Re}^{unit}_\infty$, Re_Θ, and U_∞ are the Mach number, pressure, temperature, density, unit Reynolds number, momentum-thickness Reynolds number, and velocity for each experiment.

Experiment	M_∞ (-)	P_∞ (Pa)	T_∞ (K)	ρ_∞ (kg/m^3)	$\mathrm{Re}^{unit}_\infty$ (1/m)	Re_Θ (-)	U_∞ (mm/μs)	$10\tau_m$ (μs)	x_m (mm)
M3 AEDC - 19.1 mm OP	2.77	1010	118	0.030	2.30e6	1750	0.612	4.1	2.5

beam-splitter mount was rotated slightly about the vertical axis. The two beams were directed into the test section with 1 inch 5th-harmonic Nd:YAG laser mirrors (IDEX Y5-1025-45) and focused to several narrow waists in the test section with a $f = 100$ mm fused-silica microlens array (SUSS MicroOptics Nr. 18-00127) to form the lines in the streamwise direction and a $f = 100$ mm fused-silica cylindrical lens to focus the lines in the spanwise direction. Neglecting losses from the mirrors, lenses, and windows, we estimate that the energy per write line is approximately 300 µJ/pulse.

The read laser consisted of a frequency doubled Quanta Ray Pro-350 Nd:YAG laser and a Sirah PrecisionScan Dye Laser. The Nd:YAG laser pumped the dye laser with 215 mJ/pulse at a wavelength of 532 nm. The dye in the laser was Styryl 8 with a DMSO solvent, and the laser was tuned to output a 769.5 nm beam.

The read-laser beam setup resulted in approximately 5 mJ/pulse, with a wavelength of 769.5 nm, a linewidth of approximately 0.025 cm^{-1}, a pulsewidth of approximately 7 ns, and a repetition rate of 10 Hz. The read-laser beam was directed into the test section using 2 inch broadband dielectric mirrors (Thorlabs BB2-E02), and expanded to a beam of $\approx$ 40 mm diameter with a $f = -400$ mm fused silica cylindrical lens. This "read beam" re-excites the metastable krypton tracer atoms so that their displacement can be measured.

The laser and camera timing are controlled by a pulse-delay generator (SRS DG645). The intensified camera used for all experiments is a 16-bit Princeton Instruments PIMAX-4 1024x1024 with an 18-mm grade 1, Gen III extended red filmless intensifier with P46 phosphor (PM4-1024i-HR-FG-18-P46-CM). The lens used is a Nikon NIKKOR 24-85mm f/2.8-4D in "macro" mode and positioned approximately 200 mm from the write/read location. Two high-precision 800 nm longpass filters (Thorlabs FELH0800, transmission of 3.5e-4% at the read-laser wavelength of 769.5 nm) are placed in series between the lens and the intensifier to minimize the noise resulting from the read-laser pulse reflection and scatter from solid surfaces. The gain is set to 100% with no pixel binning and only recording the read images to ensure a 10 Hz frame rate. A set of write images were recorded with the tunnel off prior to each run. The camera gate was opened for 50 ns immediately following the read-laser pulse to capture the spontaneous emission of $5p[3/2]_1 \rightarrow 5s[3/2]^o_1$ (829.8 nm) transitions.

The beams enter the test section in the same plane and intersect at $\approx$ 140 degrees. Three sets of images were performed with the wedge test article, where the position of the wedge was varied to acquire data before and after the shock. In each set, roughly 600 frames were collected.

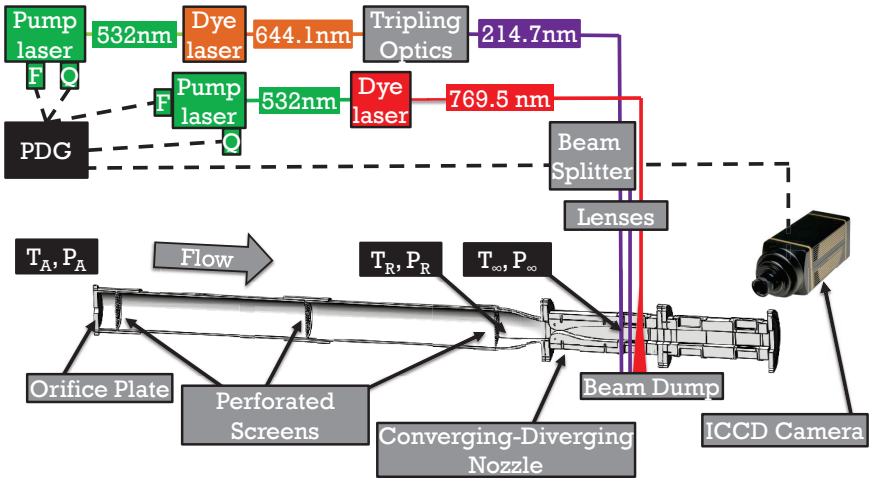

Figure 2: Schematic of KTV-2D experimental setup.

B. Optical Flow Method

Optical flow is a well known problem in computer vision which involves computing the motion of objects in an image sequence. Optical flow belongs to the class of ill-posed inverse problems and is typically solved by minimizing a constrained equation to yield the displacement field over the entire image domain. While solutions were originally formulated to resolve the motion of rigid objects in a scene following the seminal work of Horn & Schunck,[23] optical flow methods have since been applied to fluid flows.[24–31] In these

applications, optical flow solves for the displacement between two images separated by a known time interval Δt of some flow tracer. The time interval allows the displacement to be interpreted as velocity, and optical flow methods for fluid flow velocimetry are called optical flow velocimetry (OFV) methods. The flow tracer can be particles illuminated by a laser sheet as in PIV, a fluorescent dye or chemical species (i.e., PLIF), or some other flow marker.

OFV methods typically solve some version of a displaced frame difference (DFD) equation, given by

$$I_0\left(\underline{x}\right) - I_1\left(\underline{x} + \underline{u}\left(\underline{x}\right)\Delta t\right) = 0. \tag{1}$$

I_0 and I_1 are the first and second images in an image pair, pixel locations are represented by $\underline{x}$, and the unknown two-component velocity field is $\underline{u}\left(\underline{x}\right)$. This equation simply states that, under stable lighting conditions, the only differences between I_0 and I_1 are due to the transport of image intensity, or brightness, by $\underline{u}$. Equation (1) has been shown to be equivalent to that of transport of a passive scalar in fluid mechanics by Liu and Shen.[29] As mentioned above, Eq. (1) is typically solved by forming a minimization problem and employing some constraint on the velocity field because of the ill-posedness of the inverse problem. Many forms of the constraint have been employed, depending on the application, but most penalize first- or second-order derivatives of the velocity field.

A subset of OFV methods are wavelet-based OFV, or wOFV methods.[13,14,32–34] wOFV methods apply an implicit constraint on the velocity field by solving for the wavelet coefficients of the velocity field $\underline{\psi}$, instead of the velocity field directly, and enforcing a degree of sparsity on the wavelet decomposition. The resulting minimization equation is

$$\underline{\hat{u}} = \underset{\underline{\psi}}{\operatorname{argmin}} \;\; J_D\left(I_0, I_1, \underline{\psi}\right) + \lambda J_R\left(\underline{\psi}\right). \tag{2}$$

J_D is a data term based on Eq. (1) that penalizes mismatch between the first image $I_0\left(\underline{x}\right)$ and a warped second image $I_1\left(\underline{x} + \underline{u}\left(\underline{x}\right)\Delta t\right)$, J_R is a regularization term that forces the solved velocity field to exhibit fluid-like motion by imposing smoothness, and λ is a scalar parameter that balances the two terms. Further details on the wOFV algorithm applied in this work are given by Schmidt and Sutton.[14]

C. Image Preprocessing

In order for optimal processing with wOFV, the write and read images should be as similar as possible. Ideally, the only difference between them should be displacement produced by the flow, consistent with Eq. (1). Unlike the write images, the read images in tagging velocimetry methods cannot be averaged to boost SNR, and so their quality is somewhat poor compared to the write images. This necessitates substantial image pre-processing of the read images in order to apply wOFV. In this work, the read images are processed by a series of steps which (1) denoise the images by smoothing the gradients in image intensity over the image via total variation (TV) regularization using the ROF method,[35] (2) normalize the intensity along the height of the image (y-axis) to more closely match the write image intensity profile, and (3) set all pixels below a minimum light intensity threshold to zero. This process balances eliminating noise with losing as little information as possible in the form of pixel intensities.

TV regularization is a variational image denoising method that is based on a total variation prior. In the ROF method, image denoising is performed according to Eq. (3).[35]

$$\hat{I} = \underset{\hat{I}}{\operatorname{argmin}} \;\; \frac{1}{2}||I - \hat{I}||_2^2 + \sigma J(\hat{I}). \tag{3}$$

$\hat{I}$ is the denoised version of the original image I, σ is a scalar parameter that balances the first term, which penalizes differences between I and $\hat{I}$, and the second term J which is a prior function that enforces some degree of smoothness on $\hat{I}$ to reduce noise. The total variation prior has the form

$$J(\hat{I}) = \int ||\underline{\nabla}\hat{I}||\mathrm{d}\underline{x}. \tag{4}$$

The TV prior preserves edges in the image while reducing fine-scale noise. The minimization of Eq. (3) is performed using an efficient gradient descent algorithm.

The smoothing parameter σ is currently tuned using a manual process, based on qualitative image inspection. A balance is sought between reduction in image noise in the image regions away from the read lines and over-smoothing of the lines. Quantified metrics of the processed image may be analyzed in the future to automate the denoising procedure.

An example processed write, unprocessed read, and processed read image set from this experiment are shown in Fig. 3. The write and processed read image pairs were analyzed with wOFV to determine the flow

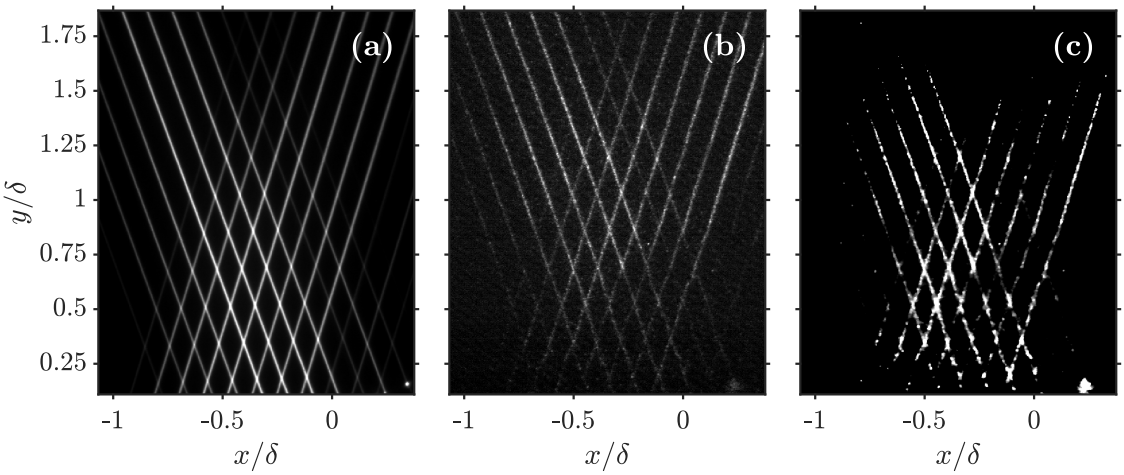

Figure 3: Example (a) write, (b) raw (unprocessed) read and (c) processed read image used for wOFV analysis. δ is the boundary layer thickness measured in a separate experiment with schlieren imaging, and the point $(x, y) = (0, 0)$ is defined as the tip of the wedge.

velocity field for each time instance. Data from individual image pairs, as well as ensemble quantities such as the median velocity and vorticity can then be calculated for the flow.

III. Results & Discussion

This section is divided into two parts. In Sec. A, images from the KTV-2D experiments of the turbulent SWBLI described in Sec. A are analyzed using wOFV and cross-correlation. Subsequently in Sec. B, synthetic KTV-2D images are produced and analyzed with wOFV in order to evaluate the performance of the method more comprehensively and estimate uncertainty in the calculated velocity fields.

A. Experiment

The velocity field was computed for a set of 54 read images from the experiment described in Sec. A. The images are cropped to the region shown in Fig. 3, which is 623×521 pixels, and a velocity vector is computed at each pixel. The instantaneous velocity field from the write and read images shown in Fig. 3 is shown in Fig. 4. The excitation lines from the write image are overlaid to aid the eye. The velocity magnitude is represented by the coloration, and individual velocity vectors are shown in green. The vectors are sub-sampled by a factor of 20 in both directions for clarity. The wOFV method produces velocity vectors even where there are no excited krypton atoms, so there is ambiguity at those points when considering only the image intensity data. Velocities at these points are computed instead by enforcing smoothness on the velocity field via J_R in Eq. (2). While obviously erroneous away from the region in the bottom-center of the image, where there are no lines or intersections, the correct qualitative trend for a turbulent boundary layer of decreasing velocity as one moves toward the wall is observed where the density of lines and intersections is high, $0.25 < y/\delta < 1$ and $-0.5 < x/\delta < -0.1$.

The mean velocity field $\bar{\underline{u}}$ can be computed from the instantaneous velocity fields $\underline{u}$, and the result is compared to the mean velocity field computed using the previous methodology of Mustafa et al.[36] in Fig. 5a. Only data from the valid intersection points as determined by the analysis of Mustafa et al. are shown for both methods for an easier comparison. Excellent agreement is observed between the two processing approaches, indicating that the vectors produced by wOFV, at least at the points of intersection, are reliable.

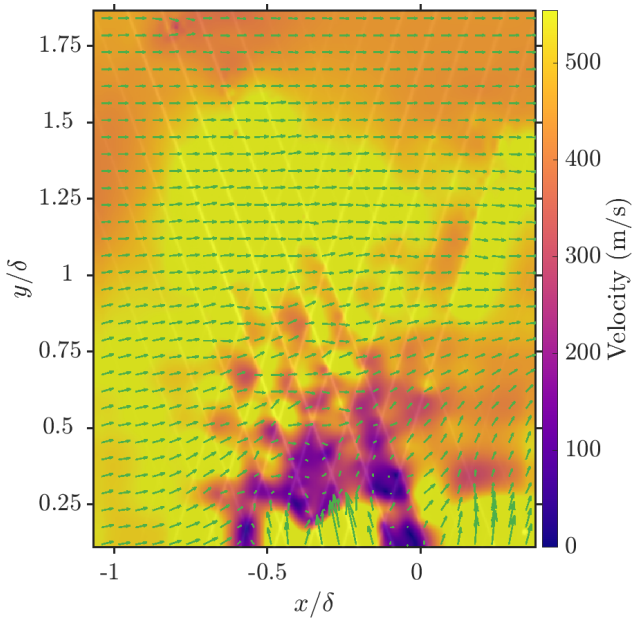

Figure 4: An instantaneous velocity field of the flow generated by the wOFV method. The excitation lines from the write image are shown overlaid on the velocity field to aid the eye. Coloration represents the velocity magnitude, and sub-sampled velocity vectors are shown in green.

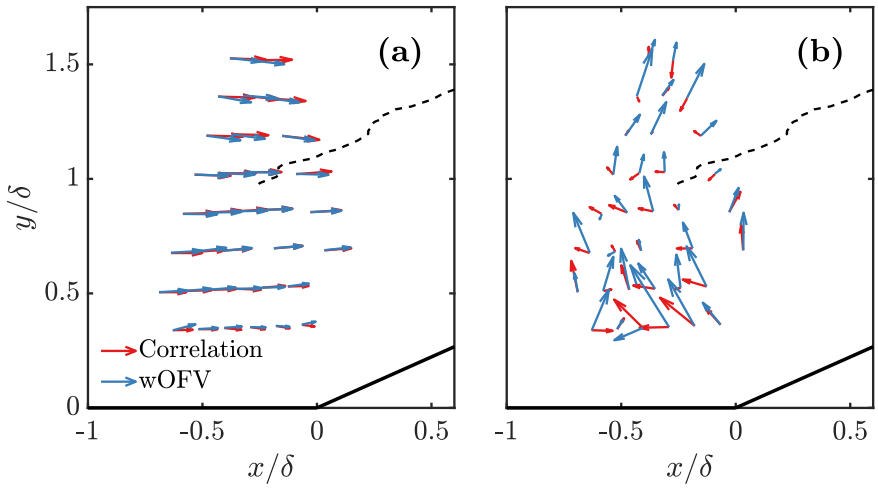

Figure 5: (a) Mean and (b) fluctuating velocity fields produced by the previous correlation-based approach[36] and the present wOFV results. The edge of the 24° wedge is shown as a solid black line in the lower-right of the figure, and the estimated shock position, determined by schlieren imaging, is shown as a dashed line. Vectors in (a) represent velocity magnitudes 4 times larger than ones of equivalent length in (b).

More interesting is the field of fluctuating velocity $\underline{u}' = \underline{u} - \bar{\underline{u}}$, which is shown for the instantaneous image in Figs. 3 and 4 in Fig. 5b. The vectors have been lengthened by a factor of 4 relative to Fig. 5a in order to aid visualization. While there is agreement between wOFV and cross-correlation at a few points, significant differences are observed between the two methods in general. This is not especially surprising, as the fluctuating streamwise velocity u' and especially the wall-normal velocity v' are challenging to measure accurately in turbulent boundary layers, particularly for compressible flows. Without further study, either using experiments in a well-characterized flow such as an incompressible turbulent boundary layer on a flat plate, or using synthetic data where the true instantaneous velocities are known, it is not possible to determine which velocimetry algorithm produces more accurate results.

B. Synthetic Data

In order to better characterize the performance of the wOFV method for images typical of tagging velocimetry, a synthetic data set was produced. The set features 12 write images, composed of two groups of parallel lines which intersect on a 512 × 512-pixel domain. The angle and spacing of the lines are varied independently over ranges representative of experimental tagging velocimetry images. The lines are assigned Gaussian intensity profiles to simulate laser excitation. An example synthetic write image is shown in Fig. 6a.

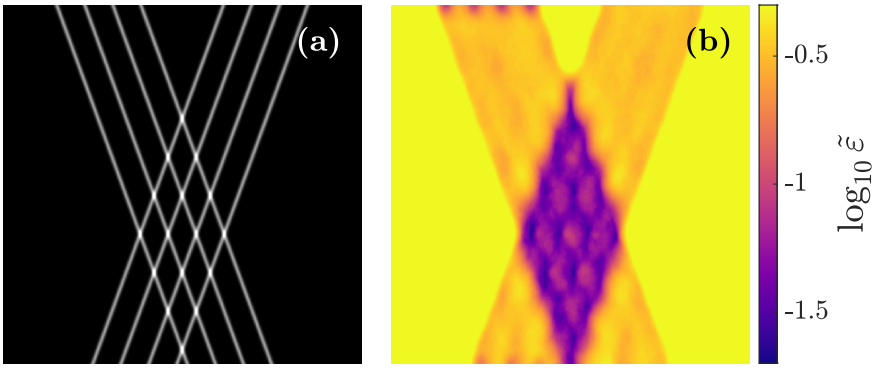

Figure 6: (a) An example write image and (b) the resulting median of the relative error magnitude.

100 individual read images were produced from each write image by advecting the write image with 100 realizations of a simulated turbulent flow. The simulated flow has a mean horizontal velocity of 5 pixels and no mean vertical velocity. The turbulence is isotropic, and both components of the velocity field follow normal distributions with standard deviations of 0.5 pixels. Each of the 1200 pairs of write and read images were processed with wOFV, and the results are compared with the known specified velocity fields. The error is quantified by computing the length of the error vector at each point and normalizing by the length of the true velocity vector:

$$\varepsilon = \frac{||\underline{u}_{\text{meas}} - \underline{u}_{\text{true}}||_2}{||\underline{u}_{\text{true}}||_2}. \tag{5}$$

$||\cdot||_2$ denotes the Euclidean norm for two-dimensional vector fields. Since all the write images in an 100-image sequence are identical, statistics can be computed for the relative error magnitude at each pixel in the image domain. Figure 6b shows the median of the relative error magnitude, denoted $\tilde{\varepsilon}$, at every point in the image domain for the write image shown in Fig. 6a. The diamond-shaped region formed by the intersections of the lines is clearly visible in the image of the error, and the median error is observed to be less than 5% in the immediate vicinity of the intersections. It is slightly higher in the regions between intersections, but still less than 10%, indicating that wOFV is capable of providing accurate velocity estimations even in regions where there is no image intensity information, as long as there are nearby image features that can be used for velocimetry. Outside of the central "diamond," the median error is considerably higher, but still reasonably small in the regions near the lines, about 30-35%. It is postulated that the error in the component normal to the line may be considerably smaller than the component parallel to the lines because of the so-called "aperture problem" in image-based motion estimation, which refers to the ambiguity in the component of motion along an isocontour of the image intensity pattern,[37] but that was not evaluated in the present work.

The pattern formed by the relative error field in Fig. 6b indicates that the error at a point in the image domain is likely a function of the Euclidean distance to the nearest intersection of write lines. Figure 7a shows a joint probability density function (PDF) of the relative error magnitude ε and the minimum distance to an intersection in the write image, i.e. the distance to the nearest intersection, for all 1200 combinations of write images and velocity fields. The population of error values shows an increasing trend with increasing distance, and the two populations are positively correlated with a computed Spearman's correlation coefficient of $r = 0.53$, indicating a reasonably strong correlation. Figure 7b further quantifies the relationship between error magnitude and distance to an intersection, as it shows the conditional median of the error as a function of minimum distance to an intersection. This curve can be thought of as taking vertical slices through the PDF in Fig. 7a and computing the median of the resulting distribution along each slice. The conditional

median in Fig. 7b can be used to create an estimate of the uncertainty in a wOFV velocity calculation for a tagging velocimetry image based on the distribution of write lines.

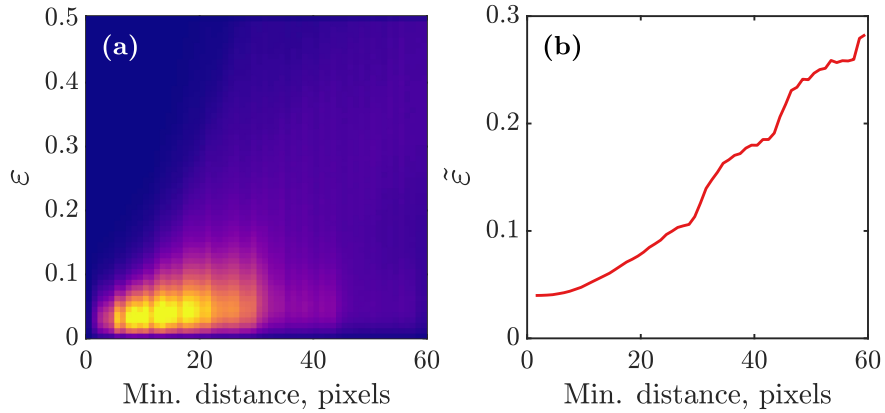

Figure 7: (a) The joint probability density function of relative error magnitude and the distance to the nearest intersection of write lines. (b) The conditional median of the relative error magnitude as a function of distance to the nearest write line intersection.

In addition to the magnitude of the error vectors, also of great interest for turbulent flows is the error in fluctuating and derivative properties of the velocity field. Specifically, the fluctuating velocity components u' and v', along with the vorticity ω, are analyzed in the present study. The top row of Fig. 8 shows the median relative error magnitude in each of the three specified quantities, organized as u', v', and ω from left to right in the figure. Note that unlike Fig. 6b, the coloration is presented on a linear scale instead of a logarithmic scale. The error in u' is relatively low, below 20%, in the immediate vicinity of intersection points, but increases sharply to over 50% only a few pixels away in the regions between them. The error is very high outside of the central diamond region. The relative error in v' is of a similar magnitude to that in u' near the intersections, but the measurements are less accurate by comparison outside the immediate vicinity of the intersections. The relative error in the vorticity is higher on average than that of u' and v' inside the diamond region, about 50-60%, but is observed to be less sensitive to the location in terms of the vicinity to the intersection points, and similar error magnitudes are observed in the vorticity outside of the diamond along the write lines, indicating that isolated write lines are able to produce vorticity measurements with similar accuracy to intersections of lines.

The bottom row of Fig. 8 shows the PDFs of the signed relative error in each quantity, computed over the region in the center of the diamond indicated by a green rectangle in the plots in the top row of the figure. For a quantity X, the signed relative error is defined as

$$\varepsilon_X^{\text{sgn}} = \frac{X_{\text{meas}} - X_{\text{true}}}{X_{\text{true}}}. \tag{6}$$

This error metric can be positive or negative. A positive value means that the magnitude of X, regardless of the sign of X_{true}, is over-estimated, and a negative value means that the magnitude of X is underestimated. While the signed error in u' is approximately centered on 0, indicating that u' is equally likely to be over- or underestimated by wOFV, the distributions for the error in both v' and ω are centered at nonzero values. The results show that v' tends to be overestimated, while ω is underestimated.

The difference in behavior between the estimations of u' and v' may be due to the fact that while the true values of u' and v' have similar magnitudes in the simulated flow, $\bar{u} = 4$ while $\bar{v} = 0$. This means that on average the vertical displacements between images are much smaller in magnitude than the horizontal displacements, and the accuracy of wOFV methods is known to depend on the displacement magnitude.[13] It is possible that wOFV's estimations of the smaller vertical component of velocity are less precise than those of the horizontal component and are biased toward larger values, leading to the observed behavior for the error in v' in Fig. 8e. Alternatively, the difference could be due to the inclination of the write lines, which are closer to vertical than horizontal in all of the write images tested. As mentioned previously, wOFV is expected to be more precise when estimating the velocity component normal to the write lines than the component parallel to the lines due to the aperture problem, which would imply more precision in estimating the horizontal component of velocity than the vertical component.

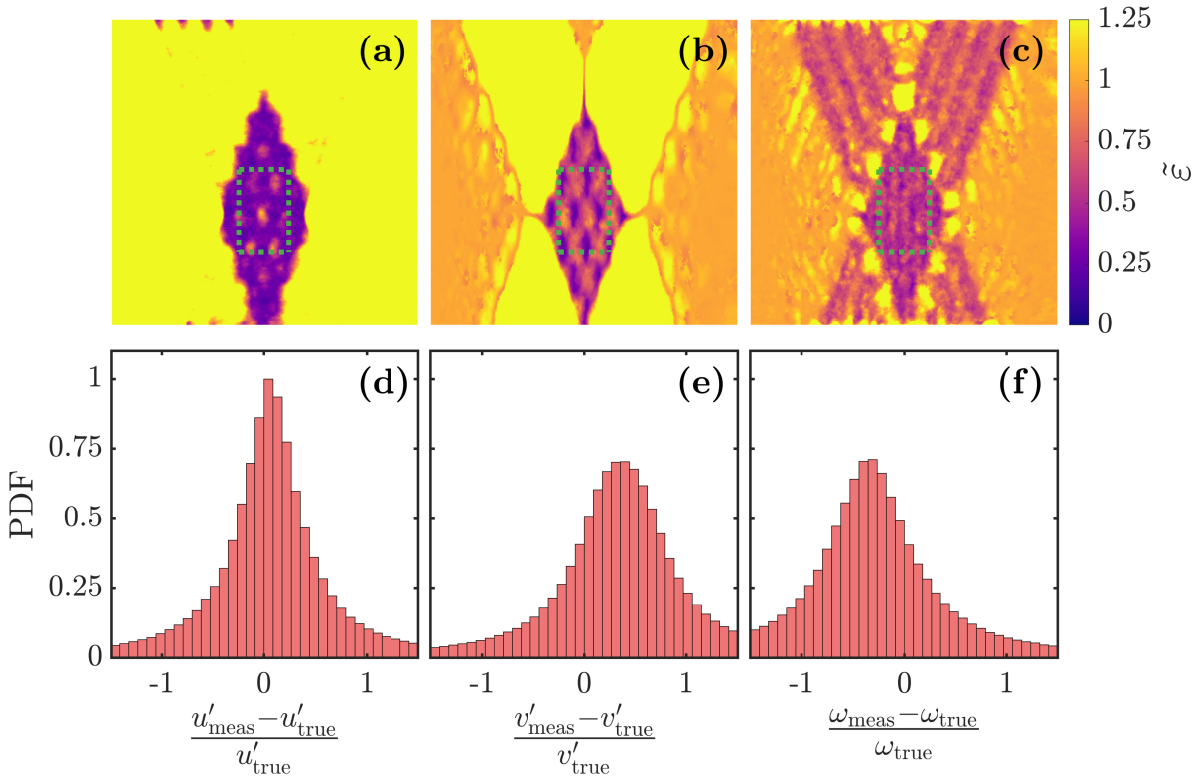

Figure 8: Top: Median relative error magnitude in (a) u', (b) v', and (c) ω. Bottom: The PDFs of the signed relative error in (d) u', (e) v', and (f) ω computed over the central region of the image domain marked with a green rectangle in the top row of the figure.

Unlike u' and v', which are temporally fluctuating quantities, ω is a function of spatial variations in the velocity vector field. The fact that it tends to be underestimated indicates that the estimated velocity field is over-smoothed, i.e. low-pass filtered. The amount of smoothing in wOFV is controlled by λ, and a smaller value of λ would result in less smoothing, and therefore likely a more accurate estimation of the vorticity, albeit with the potential sacrifice of some accuracy away from the write line intersection points where smoothness in the velocity field strongly informs the velocity estimation. It should also be pointed out here that spatial derivative quantities, such as vorticity and strain rate, along with spatial turbulence spectra, are known to be low-pass filtered by other velocimetry techniques such as PIV, even in low Mach number flows where particle lag is not appreciable. This is due to the finite width of interrogation windows used for cross-correlation in PIV, and the effect is strongly illustrated for PIV in a turbulent flame by Schmidt et al.[38]

IV. Conclusions & Future Work

wOFV was applied in this work to two sets of tagging velocimetry image data in order to evaluate its performance. The first set of images were acquired in an experiment of a turbulent shock wave-boundary layer interaction in a Mach 2.75 free stream flow using KTV-2D. An image denoising procedure using total variation (TV) regularization was applied to the experimental read images in order to boost the SNR and produce more reliable velocity estimations. Good agreement is observed between velocity estimations using wOFV and cross-correlation for the mean velocity field, but wOFV has several distinct advantages. First, as an automated process, wOFV is much simpler to implement and more adaptable than the cross-correlation procedure employed, which requires significant manual tuning in order to identify line intersection locations. Second, wOFV produces a velocity estimation at every point in the image domain, instead of only at line intersection points, and can therefore provide a more complete picture of the turbulent velocity field as well as potentially enabling the straightforward computation of spatial turbulence spectra and derivative

quantities such as vorticity. Less agreement is observed between wOFV and cross-correlation for the velocity fluctuations, but it is unknown at this time which method is more accurate.

A second set of synthetic data was produced to further quantify the accuracy of wOFV applied to tagging velocimetry images. A high degree of accuracy is observed in terms of the magnitude of the error vectors, with errors between 2 and 5% near the intersections of write lines. Error is found to correlate positively with the distance from intersection locations. Measurements of the velocity fluctuations and vorticity are less accurate, and the vertical velocity fluctuation magnitude is more often overestimated than underestimated, unlike the horizontal fluctuations, which are equally likely to be over- or underestimated. This is postulated to be due to either the difference between the mean velocity in each direction or the inclination of the write lines. The vorticity magnitude tends to be underestimated, likely resulting from a low-pass filtering effect of the regularization parameter λ in wOFV computation. It is possible that there is a tradeoff between the accuracy of the estimation of vorticity and the accuracy at points away from the line intersections, depending on the value of λ chosen. It is important to note that the synthetic images in the present work are ideal–they have zero noise, and the only change between the write and read images is the transport of image intensity due to flow advection. Therefore the error analysis in Sec. B represents a lower bound on the error, as imaging noise and other effects are likely to increase the errors in wOFV estimation.

Further experimental and numerical work is warranted to better understand the performance of wOFV in tagging velocimetry applications so that it can be applied more broadly. In order to better quantify the accuracy of wOFV compared to cross-correlation in experiments, tagging velocimetry images should be acquired in well-characterized flows, such as incompressible flat-plate boundary layers. In addition, the application of wOFV to traditional one-dimensional tagging velocimetry images such as those in [39–41] is of great interest. A great number of additional analyses using synthetic data could be performed. Larger populations of velocity fields than the ones in the present study should be produced to better converge statistics of the fluctuation quantities. An infinite number of combinations of simulated flows and image patterns can be produced, allowing more tailored analyses of synthetic data resembling a desired experimental configuration. This could include recent developments such as write images featuring Talbot effect patterns,[42] as well as quantifying the error in the velocity components normal and parallel to the write lines. Finally, imaging noise should be simulated to quantify the effects of noise on the accuracy of wOFV, and the wOFV results on simulated data should be compared to those of cross-correlation to compare the accuracy of the two methods.

Acknowledgments

The experimental data used in this work were acquired in the Mach 3 Calibration Tunnel at the Arnold Engineering Development Complex (AEDC). The Air Force SFFP supported Mustafa and Parziale with a stipend for this work. Mustafa and Parziale were supported by AFOSR Young Investigator Program Grant FA9550-16-1-0262, and equipment for this work was supported by AFOSR DURIP Grants FA9550-15-1-0325 and FA9550-19-1-0182. Shekhtman was supported by ONR Young Investigator Research Program Grant N00014-20-1-2549, AF SBIR grants FA9101-17-P-0094 and FA2487-19-C-0013, and ONR DURIP grants N00014-19-1-2523 and N00014-20-1-2637.

References

[1]Smits, A. J. and Dussauge, J.-P., *Turbulent Shear Layers in Supersonic Flow*, Springer, 2006.

[2]Clemens, N. T. and Narayanaswamy, V., "Low-Frequency Unsteadiness of Shock Wave/Turbulent Boundary Layer Interactions," *Annual Review of Fluid Mechanics*, Vol. 46, No. 1, 2014, pp. 469–492.

[3]Tropea, C., "Laser Doppler anemometry: recent developments and future challenges," *Measurement Science and Technology*, Vol. 6, No. 6, 1995, pp. 605–619.

[4]Raffel, M., Willert, C. E., Scarano, F., Kähler, C. J., Wereley, S. T., and Kompenhans, J., *Particle image velocimetry: a practical guide*, Springer, 2018.

[5]Melling, A., "Tracer particles and seeding for particle image velocimetry," *Measurement Science and Technology*, Vol. 8, 1997, pp. 1406–1416.

[6]Loth, E., "Compressibility and Rarefaction Effects on Drag of a Spherical Particle," *AIAA Journal*, Vol. 46, No. 9, 2008, pp. 2219–2228.

[7]Koochesfahani, M. M. and Nocera, D. G., "Molecular tagging velocimetry," *Handbook of Experimental Fluid Dynamics*, 2007, pp. 362–382.

[8]Parziale, N. J., Smith, M. S., and Marineau, E. C., "Krypton tagging velocimetry of an underexpanded jet," *Applied*

Optics, Vol. 54, No. 16, 2015, pp. 5094–5101.

[9]Mustafa, M. A., Parziale, N. J., Smith, M. S., and Marineau, E. C., "Two-Dimensional Krypton Tagging Velocimetry (KTV-2D) Investigation of Shock-Wave/Turbulent Boundary-Layer Interaction," *Proceedings of AIAA SciTech 2018*, AIAA-2018-1771, Kissimmee, Florida, 8-12 January 2018.

[10]Gendrich, C. P. and Koochesfahani, M. M., "A spatial correlation technique for estimating velocity fields using molecular tagging velocimetry (MTV)," *Experiments in Fluids*, Vol. 22, No. 1, 1996, pp. 67–77.

[11]Ramsey, M. C. and Pitz, R. W., "Template matching for improved accuracy in molecular tagging velocimetry," *Experiments in Fluids*, Vol. 51, No. 3, 2011, pp. 811–819.

[12]Sánchez-González, R., McManamen, B., Bowersox, R. D. W., and North, S. W., "A method to analyze molecular tagging velocimetry data using the Hough transform," *Review of Scientific Instruments*, Vol. 86, 2015, pp. 105106.

[13]Schmidt, B. E. and Sutton, J. A., "High-resolution velocimetry from tracer particle fields using a wavelet-based optical flow method," *Experiments in Fluids*, Vol. 60, No. 37, 2019.

[14]Schmidt, B. E. and Sutton, J. A., "Improvements in the accuracy of wavelet-based optical flow velocimetry (wOFV) using an efficient and physically based implementation of velocity regularization," *Experiments in Fluids*, Vol. 61, No. 2, 2020.

[15]Schmidt, B. E., Towery, C. A. Z., Hamlington, P. E., and Sutton, J. A., "Evaluation of wavelet-based optical flow velocimetry from OH scalar fields in reacting turbulent flows," *AIAA Scitech 2019 Forum*, No. AIAA 2019-0270, 2019.

[16]Zahradka, D., Parziale, N. J., Smith, M. S., and Marineau, E. C., "Krypton tagging velocimetry in a turbulent Mach 2.7 boundary layer," *Experiments in Fluids*, Vol. 57, 2016, pp. 62.

[17]Mustafa, M. A., Parziale, N. J., Smith, M. S., and Marineau, E. C., "Nonintrusive Freestream Velocity Measurement in a Large-Scale Hypersonic Wind Tunnel," *AIAA Journal*, Vol. 55, No. 10, 2017, pp. 3611–3616.

[18]Mustafa, M. A., Parziale, N. J., Smith, M. S., and Marineau, E. C., "Amplification and structure of streamwise-velocity fluctuations in compression-corner shock-wave/turbulent boundary-layer interactions," *Journal of Fluid Mechanics*, Vol. 863, 2019, pp. 1091–1122.

[19]Mustafa, M. A. and Parziale, N. J., "Simplified read schemes for krypton tagging velocimetry in N_2 and air," *Optics Letters*, Vol. 43, No. 12, 2018, pp. 2909–2912.

[20]Mustafa, M. A., Shekhtman, D., and Parziale, N. J., "Single-Laser Krypton Tagging Velocimetry Investigation of Supersonic Air and N_2 Boundary-Layer Flows over a Hollow Cylinder in a Shock Tube," *Physical Review Applied*, Vol. 11, No. 6, 2019, pp. 064013.

[21]Shekhtman, D., Mustafa, M. A., and Parziale, N. J., "Two-photon cross-section calculations for krypton in the 190-220 nm range," *Applied Optics*, Vol. 59, No. 34, 2020, pp. 10826–10837.

[22]Chang, R. S. F., Horiguchi, H., and Setser, D. W., "Radiative lifetimes and two-body collisional deactivation rate constants in argon for $Kr(4p^55p)$ and $Kr(4p^55p')$ states," *The Journal of Chemical Physics*, Vol. 73, No. 2, 1980, pp. 778–790.

[23]Horn, B. K. P. and Schunck, B. G., "Determining Optical Flow," *Artificial Intelligence*, Vol. 17, 1981, pp. 185–203.

[24]Tokumaru, P. T. and Dimotakis, P. E., "Image correlation velocimetry," *Experiments in Fluids*, Vol. 19, 1995, pp. 1–15.

[25]Yuan, J., Schnörr, C., and Mémin, E., "Discrete Orthogonal Decomposition and Variational Fluid Flow Estimation," *Journal of Mathematical and Imaging Vision*, Vol. 28, 2007, pp. 67–80.

[26]Corpetti, T., Mémin, E., and Pérez, P., "Dense Estimation of Fluid Flows," *IEEE Transactions on Pattern Analysis and Machine Intelligence*, Vol. 24, No. 3, March 2002, pp. 365–380.

[27]Corpetti, T., Heitz, D., Arroyo, G., Mémin, E., and Santa-Cruz, A., "Fluid experimental flow estimation based on an optical-flow scheme," *Experiments in Fluids*, Vol. 40, No. 1, 2006, pp. 80–97.

[28]Chen, X., Zillé, P., Shao, L., and Corpetti, T., "Optical flow for incompressible turbulence motion estimation," *Experiments in Fluids*, Vol. 56, No. 8, 2015.

[29]Liu, T. and Shen, L., "Fluid flow and optical flow," *Journal of Fluid Mechanics*, Vol. 614, 2008, pp. 253–291.

[30]Liu, T., "OpenOpticalFlow: An Open Source Program for Extraction of Velocity Fields from Flow Visualization Images," *Journal of Open Research Software*, Vol. 5, No. 1, 2017.

[31]Cai, S., Mémin, E., Dérian, P., and Xu, C., "Motion estimation under location uncertainty for turbulent fluid flows," *Experiments in Fluids*, Vol. 59, No. 8, 2018.

[32]Kadri-Harouna, S., Dérian, P., Héas, P., and Mémin, E., "Divergence-free wavelets and high order regularization," *International Journal of Computer Vision*, Vol. 103, No. 1, 2013, pp. 80–99.

[33]Dérian, P., Héas, P., Herzet, C., and Mémin, E., "Wavelets and Optical flow motion estimation," *Numerical Mathematics: Theory, Methods and Applications*, Vol. 6, 2013, pp. 116–137.

[34]Dérian, P. and Almar, R., "Wavelet-based optical flow estimation of instant surface currents from shore-based and UAV videos," *IEEE Transactions on Geoscience and Remote Sensing*, Vol. 55, No. 10, 2017, pp. 5790–5797.

[35]Rudin, L. I., Osher, S., and Fatemi, E., "Nonlinear total variation based noise removal algorithms," *Physica D: Nonlinear Phenomena*, Vol. 60, No. 1-4, 1992, pp. 259–268.

[36]Mustafa, M. A., Parziale, N. J., Marineau, E. C., and Smith, M. S., "Two-Dimensional Krypton Tagging Velocimetry (KTV-2D) Investigation of Shock-Wave/Turbulent Boundary-Layer Interaction," *2018 AIAA Aerospace Sciences Meeting*, 2018.

[37]Ullman, S., *The interpretation of visual motion*, Massachusetts Inst of Technology Pr, 1979.

[38]Schmidt, B. E., Skiba, A. W., Hammack, S. D., Carter, C. D., and Sutton, J. A., "High-resolution velocity measurements in turbulent premixed flames using wavelet-based optical flow velocimetry (wOFV)," *Proceedings of the Combustion Institute*, 2020.

[39]Zahradka, D., Parziale, N. J., Smith, M. S., and Marineau, E. C., "Krypton tagging velocimetry in a turbulent Mach 2.7 boundary layer," *Experiments in Fluids*, Vol. 57, No. 5, 2016.

[40]Mustafa, M. A., Parziale, N. J., Smith, M. S., and Marineau, E. C., "Nonintrusive Freestream Velocity Measurement in a Large-Scale Hypersonic Wind Tunnel," *AIAA Journal*, Vol. 55, No. 10, 2017, pp. 3611–3616.

[41]Mustafa, M. A., Parziale, N. J., Smith, M. S., and Marineau, E. C., "Amplification and structure of streamwise-velocity fluctuations in compression-corner shock-wave/turbulent boundary-layer interactions," *Journal of Fluid Mechanics*, Vol. 863, 2019, pp. 1091–1122.

[42]Fort, C., André, M. A., Pazhand, H., and Bardet, P. M., "Talbot-effect structured illumination: pattern generation and application to long-distance μ-MTV," *Experiments in Fluids*, Vol. 61, No. 2, 2020.